

# An Investigation into the Charge Storage Mechanism and Cycling Performance of $\text{Mn}_2\text{O}_3$ as the Cathode Material for Zinc-Ion Batteries

Qingping Hou<sup>[a]</sup> and Douglas G. Ivey\*<sup>[a]</sup>

In this work, highly crystalline, nanosize  $\text{Mn}_2\text{O}_3$  powder is synthesized via a precipitation and calcination method for utilization as the cathode in aqueous zinc-ion batteries (aZIBs). The resultant electrodes are characterized using electrochemical and microstructural methods to determine the mechanisms associated with charge and discharge. In addition, a few quantitative testing methods are used to investigate cycling performance stability. A specific capacity of  $211 \text{ mAh g}^{-1}$  is retained after 200 cycles at a current density of  $500 \text{ mA g}^{-1}$  with

93% capacity retention. Also, 73% capacity retention can be reached after 1100 cycles at  $2000 \text{ mA g}^{-1}$ . The energy storage mechanism associated with  $\text{Mn}_2\text{O}_3$  is for the first time proposed to be a chemical conversion reaction type with two steps involving the formation/decomposition of  $\text{ZnMn}_2\text{O}_4$  (hetaerlite) and zinc sulphate hydroxide (ZHS). Also, capacity fading is directly linked to the incomplete reversibility of the chemical conversion reaction mechanism.

## Introduction

Easily exploitable traditional fossil fuels are being depleted and they contribute to the decline in air quality.<sup>[1]</sup> Therefore, it is imperative to develop new, efficient, clean, and sustainable energy sources to replace traditional sources.<sup>[2,3]</sup> Batteries have been widely studied as energy devices that can convert chemical energy into electrical energy. Currently, the most widely used batteries include lithium-ion batteries,<sup>[4]</sup> lead-acid batteries,<sup>[5]</sup> and nickel-cadmium batteries.<sup>[6]</sup> These batteries all have some shortcomings, which limit their usage. For example, lithium-ion batteries have cost, safety, and environmental issues, as well as potentially limited supplies of lithium.<sup>[7]</sup> Lead-acid batteries have low specific energy density, poor cycle performance, and environmental problems.<sup>[8]</sup> Nickel-cadmium batteries exhibit a memory effect and have environmental issues.<sup>[9]</sup> As such, none of these batteries fully satisfy the requirements of a secondary battery.

Secondary aqueous ion batteries have attracted researchers' attention due to their low cost, long cycle life, and safe operation. These batteries utilize an aqueous solution as the electrolyte; the aqueous electrolyte is safe, easy to prepare, and has high ionic conductivity. Therefore, secondary aqueous ion batteries are considered as promising candidates for large-scale energy storage. In the past ten years, secondary aqueous ion batteries have received increasing attention for application in the power grid and for wearable devices and biocompatibility.<sup>[10,11]</sup>

Manganese oxide is widely used in various industries, for applications such as deoxidization and desulfurization, catalysis, and batteries, due to the different oxidation states (2+, 3+, and 4+) for Mn. For battery electrode materials, the diversity of manganese oxide compositions and crystal structures make it attractive.<sup>[12,13]</sup> Manganese (4+) oxide ( $\text{MnO}_2$ ) has been widely used as the cathode material in aqueous zinc-ion batteries (aZIBs). Other oxides with different valence states, such as  $\text{Mn}_3\text{O}_4$  (2+/3+) and  $\text{Mn}_2\text{O}_3$  (3+), are also possible cathode candidates.  $\text{Mn}_2\text{O}_3$  has generated interest because of its high theoretical specific capacity and energy density. Utilization of  $\text{Mn}_2\text{O}_3$  as the cathode material in an aZIB has been reported by several research groups in recent years.<sup>[14–20]</sup> These groups report good electrochemical performance; however, the charge storage mechanism(s) for  $\text{Mn}_2\text{O}_3$  as the cathode material is not established as different groups have proposed different processes. Some examples include intercalation of  $\text{H}^+$  and/or  $\text{Zn}^{2+}$  ions as well various chemical and electrochemical reactions.

In this study, highly crystalline bixbyite  $\text{Mn}_2\text{O}_3$  is synthesized and utilized as the cathode material for aZIBs. In addition to reporting battery performance and cycling behavior, detailed electrochemical and microstructural characterization of  $\text{Mn}_2\text{O}_3$  during battery discharging and charging is carried out. The analysis is then compared with the work reported in the literature, with the aim of providing further insight into the cathode processes involved during battery operation. A new mechanism, involving only chemical conversion reactions, is proposed.

[a] Q. Hou, Prof. D. G. Ivey  
Department of Chemical and Materials Engineering  
University of Alberta  
Edmonton, Alberta, Canada T6G 1H9  
E-mail: divey@ualberta.ca

 Supporting information for this article is available on the WWW under  
<https://doi.org/10.1002/batt.202200190>

## Results and Discussion

### Structure and morphology

The crystal structure of the as prepared electrode powder was determined using X-ray diffraction (XRD – Figure 1a). All the peaks can be indexed to the bixbyite form of  $\text{Mn}_2\text{O}_3$  (JCPDS 41-1442, Figure S2). The SEM image presented in Figure 1b shows the pristine  $\text{Mn}_2\text{O}_3$  powder particles, which have an average size less than 2  $\mu\text{m}$ . X-ray photoelectron spectroscopy (XPS) was also carried out to confirm the Mn oxidation state. The Mn 3s high-resolution spectrum is shown in Figure 1c. The Mn valence was confirmed using the amount of Mn 3s peak splitting. The value of 5.44 eV corresponds to  $\text{Mn}^{3+}$  or  $\text{Mn}_2\text{O}_3$ .<sup>[21,22]</sup> The Mn 2p3/2 spectrum is also included in Figure S1 as further confirmation of the Mn oxidation state. A scanning transmission electron microscope (STEM) bright field (BF) image, along with corresponding energy dispersive X-ray spectroscopy (EDS) maps and a selected area electron diffraction (SAED) pattern (Figure 1d), confirm the XRD and XPS results.

### Electrochemical performance

Cyclic voltammetry (CV) and galvanostatic charge-discharge (GCD) cycling tests were used to determine the electrochemical performance of the as fabricated  $\text{Mn}_2\text{O}_3$  cathode material. Figure 2a shows the CV curves at a scan rate of 0.25  $\text{mV s}^{-1}$  between 1.0 and 1.9 V, with Zn foil as the reference electrode. Two pairs of oxidation/reduction peaks are present, indicating multiple stages for the charge/discharge process. The GCD profiles at current densities ranging from 50 to 2000  $\text{mA g}^{-1}$  are shown in Figure 2b. The discharge curve exhibits two apparent plateaus at 1.25–1.29 V and 1.35–1.39 V, and the charge curve exhibits plateaus at 1.53–1.55 V and 1.57–1.61 V. These plateaus correspond with the two pairs of reduction/oxidation peaks in the CV curves.

The rate performance of the electrodes was tested by cycling at multiple current densities of 50, 100, 200, 500, 1000, and 2000  $\text{mA g}^{-1}$  for 5 cycles each. As shown in Figure 2c, the highly crystalline  $\text{Mn}_2\text{O}_3$  electrode exhibits excellent rate capability. The electrode delivers discharge capacities of 375, 341, 289, 205, 113, and 65  $\text{mAh g}^{-1}$  at 50, 100, 200, 500, 1000, and 2000  $\text{mA g}^{-1}$ , respectively. Also, the capacity of the electrode returns to the original level when the lower current densities are retested, revealing good stability for the electrode. The cells in this work delivered good electrochemical performance.

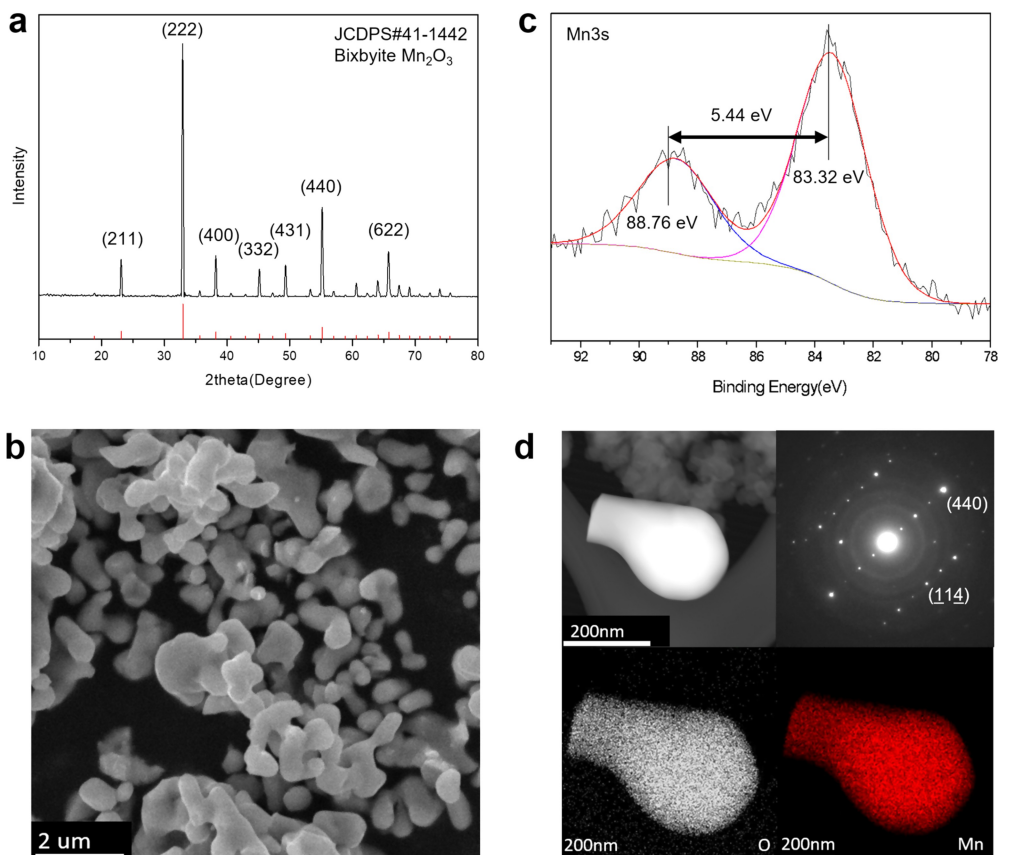


**Figure 1.** Microstructural characterization for as fabricated  $\text{Mn}_2\text{O}_3$ . a) XRD pattern; b) XPS high-resolution Mn 3s spectrum; c) SEM secondary electron (SE) image of  $\text{Mn}_2\text{O}_3$  powder; d) STEM annular dark field (ADF) image, EDS maps for Mn and O, and SAED pattern from the particle shown. The electron diffraction pattern is close to a [221] zone axis for bixbyite.

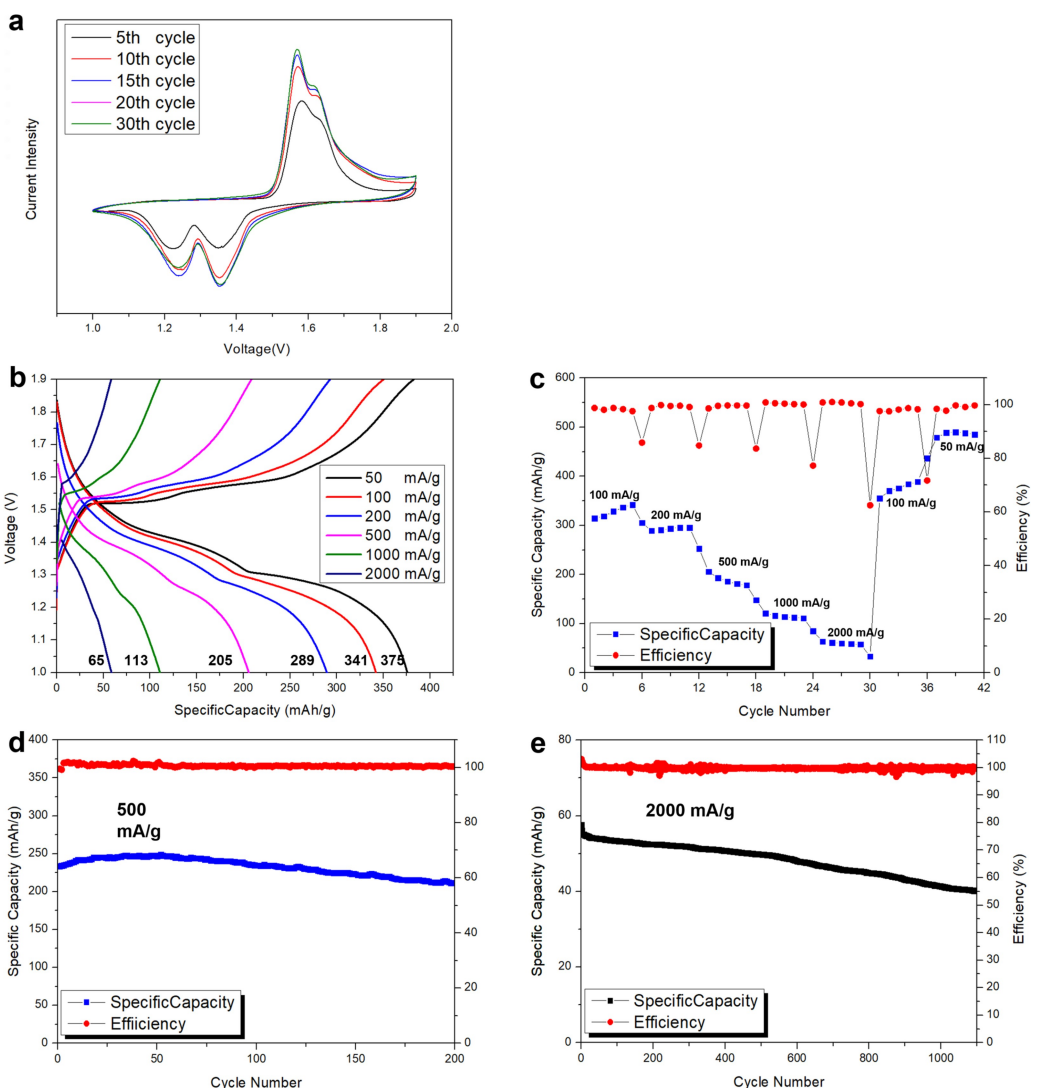


**Figure 2.** a) CV curves at  $0.25 \text{ mVs}^{-1}$ . b) GCD curves at  $50, 100, 200, 500, 1000$ , and  $2000 \text{ mA g}^{-1}$ . c) Rate capability tests at  $50, 100, 200, 500, 1000$ , and  $2000 \text{ mA g}^{-1}$  and then again at  $100$  and  $50 \text{ mA g}^{-1}$ . d) Galvanostatic charge-discharge electrochemical performance at  $500 \text{ mA g}^{-1}$  for  $200$  cycles. e) Galvanostatic charge-discharge electrochemical performance at  $2000 \text{ mA g}^{-1}$  for  $1100$  cycles.

ance, comparable to or better than previous studies (Table 1). At lower current densities, the tested single cell has discharge capacities of  $375, 341, 289$ , and  $205 \text{ mAh g}^{-1}$  at  $50, 100, 200$ , and  $500 \text{ mA g}^{-1}$ , respectively, which are better specific capacities relative to previous studies. The performance at higher current densities does not exceed values reported in previous studies, but the performance results are still competitive.

Cycle testing of the electrode was performed at current densities of  $500$  and  $2000 \text{ mA g}^{-1}$ . Figure 2d shows the cycling performance of the cell at a current density of  $500 \text{ mA g}^{-1}$  for  $200$  cycles between  $1.0$  and  $1.9 \text{ V}$ . A maximum specific capacity of  $255 \text{ mAh g}^{-1}$  can be delivered at this current rate with  $93.7\%$  retention of the original capacity after  $200$  cycles. At  $2000 \text{ mA g}^{-1}$ , the electrode has an initial capacity of  $57.2 \text{ mAh g}^{-1}$  and a final capacity at  $41.7 \text{ mAh g}^{-1}$  after  $1100$  cycles ( $73\%$  retention). The Coulombic efficiency is maintained at nearly  $100\%$  for the two test conditions, which indicates good stability for the electrode at both lower and higher

current densities. Capacity fading phenomena during cycling will be discussed in the last subsection.

### Mechanism investigation

Ex-situ XRD and SEM were carried out to investigate the charge storage mechanism for the  $\text{Mn}_2\text{O}_3$  cathode of the ZIB. Figure 3a shows the GCD curve for half of the  $15^{\text{th}}$  cycle (discharge) and the entire  $16^{\text{th}}$  cycle (charge and discharge) at a current density of  $200 \text{ mA g}^{-1}$ . The GCD curve shows two discharge and two charge plateaus for the full cycle, which suggests a two-step reaction mechanism. The discharge plateaus are separated by a “turning point” at position (d) (Figure 3a). Each of the points on the curve represents stages where the process was stopped, and the electrode was examined ex-situ via XRD and SEM. Select samples were also analyzed using TEM. Figure 3b and c,

**Table 1.** Battery cycling performance comparison for this work and previous studies of bixbyite  $\text{Mn}_2\text{O}_3$  as the cathode in ZIBs.

Specific capacity [mAh g <sup>-1</sup> ] Authors	Current density [mA g <sup>-1</sup> ]											Potential window & electrolyte	
	50–60	100	150	200	300	500	600	900	1000	1500	1800	2000	
Jiang et al. <sup>[14]</sup>		137		100	86	74			57			38	1–1.9 V 2 M $\text{ZnSO}_4$
Mao et al. <sup>[15]</sup>	225	200		175	160	145			120		100	70	0.9–1.9 V 2 M $\text{ZnSO}_4$ + 0.2 M $\text{MnSO}_4$
Feng et al. <sup>[16]</sup>	292		258		228		206			179		162	1–1.8 V 2 M $\text{ZnSO}_4$ + 0.2 M $\text{MnSO}_4$
Shen et al. <sup>[17]</sup>		190			150			130			100	85	1–1.9 V 2 M $\text{ZnSO}_4$ + 0.1 M $\text{MnSO}_4$
Ma et al. <sup>[18]</sup>	228		217					148			131	105	1–1.9 V 2 M $\text{ZnSO}_4$ + 0.1 M $\text{MnSO}_4$
This work	375	341		289		205			113		65		1–1.9 V 2 M $\text{ZnSO}_4$ + 0.2 M $\text{MnSO}_4$

Values are determined from data presented in the specific reference.

as well as Figure 4a–l, present the ex-situ XRD and SEM analysis for each stage.

Position (a) in Figure 3a corresponds to the fully charged state of the 15<sup>th</sup> cycle. The peaks in the XRD pattern (Figure 3b) can be indexed to cubic  $\alpha\text{-Mn}_2\text{O}_3$  (bixbyite) and graphitic carbon (JCPDS 75-2078 – Figure S3). The corresponding SEM image is shown in Figure 4a and is similar to the electrode morphology before testing. Positions (b) and (c) in Figure 3a show the 1<sup>st</sup> discharge plateau of the 15<sup>th</sup> cycle, which precedes the turning point. The XRD patterns in Figure 3b for positions (b) and (c) can still be indexed to  $\text{Mn}_2\text{O}_3$  and carbon, with no additional peaks. However, there is a slight change in morphology at position (c) (Figure 4c), in the form of a few small flakes, which are detectable at higher magnification. Positions (d), (e) and (f) in Figure 3a correspond to the 2<sup>nd</sup> discharge plateau. Starting at the turning point (d), in addition to the  $\text{Mn}_2\text{O}_3$  and carbon peaks, the XRD patterns show two peaks at 2-theta less than 10°. The intensities of these peaks increase significantly as discharge proceeds (positions (e) and (f)). The peak at 8.6° corresponds to the most intense peak for tetrahydrate zinc sulphate hydroxide ( $\text{Zn}_4\text{SO}_4(\text{OH})_6 \cdot 4\text{H}_2\text{O}$  or ZHS · 4H<sub>2</sub>O, JCPDS 44-0673 – Figure S4) and the peak at 9.6° corresponds to the most intense peak for trihydrate zinc sulphate hydroxide ( $\text{Zn}_4\text{SO}_4(\text{OH})_6 \cdot 3\text{H}_2\text{O}$  or ZHS · 3H<sub>2</sub>O, JCPDS 33-0689 – Figure S5). The corresponding SEM images are shown in Figure 4d–f; the formation of these two phases, hereafter referred to as ZHS, correlates with the appearance of large flakes on the electrode surface during the 2<sup>nd</sup> discharge plateau (Figure 4e). The small flakes detected at higher magnification in Figure 4c and 4d likely correspond to the initial appearance of ZHS.

Positions (g) and (h) in Figure 3a correspond to the almost fully discharged and fully discharged states of the 15<sup>th</sup> cycle. The ZHS peaks in Figure 3b continue to increase in intensity and reach maximum values at full discharge (position (h)). The corresponding SEM images in Figure 4g and h show additional

ZHS flakes. There are several additional weak peaks that appear in the XRD patterns for positions (g) and (h). These are located at about 17.5°, 19.2°, 21.5°, 27.5°, 28.8°, 34°, 37.5°, and 59° 2-theta and can be attributed to either of the two ZHS phases.

Positions (i), (j) and (k) in Figure 3a correspond to the 1<sup>st</sup> charge plateau, the 2<sup>nd</sup> charge plateau, and the fully charged state for the 16<sup>th</sup> cycle. As with the discharge process, the  $\text{Mn}_2\text{O}_3$  and carbon peaks remain (Figure 3b), while the intensities of the two strong ZHS peaks (at < 10° 2-theta) decrease during charging and completely disappear in the fully charged state, which is an indication that ZHS formation is reversible. The weak ZHS peaks also disappear. The corresponding SEM images are shown in Figure 4i–k; the number and size of ZHS flakes decrease and disappear at full charge. The morphology of the electrode in the fully charged state (Figure 4k) of the 16<sup>th</sup> cycle is also similar to the electrode morphology in the previous fully charged state and the morphology before testing. Position (l) in Figure 3a corresponds to the next fully discharged state of the 16<sup>th</sup> cycle. The two ZHS peaks reappear in the XRD pattern (Figure 3b), as do the ZHS flakes in the SEM image (Figure 4l).

The LHS of Figure 3c shows a magnified view of the 30°–50° 2-theta range for the XRD patterns for the electrodes during discharge. Pure Mn powder was added to the samples for XRD analysis to act as an internal calibration standard in order to determine any  $\text{Mn}_2\text{O}_3$  peak shifts that could arise from  $\text{Zn}^{2+}$  or  $\text{H}^+$  insertion during discharge. The (411) peak for Mn at 43.02° 2-theta (Figure S6) was used to calibrate all the patterns. On the RHS of Figure 3c, an enlarged view of the XRD patterns for the 32°–34° 2-theta range is shown. One of the major  $\text{Mn}_2\text{O}_3$  peaks at ~33.0° is visible and corresponds to the (222) plane. There appears to be a shift to lower angles starting at position (b) from 32.960° to 32.897°, which indicates the possibility of  $\text{H}^+$  and/or  $\text{Zn}^{2+}$  insertion into the  $\text{Mn}_2\text{O}_3$  crystal. Any ion insertion should increase the d-spacing or reduce the Bragg angle. However, the maximum amount of d-spacing shift for

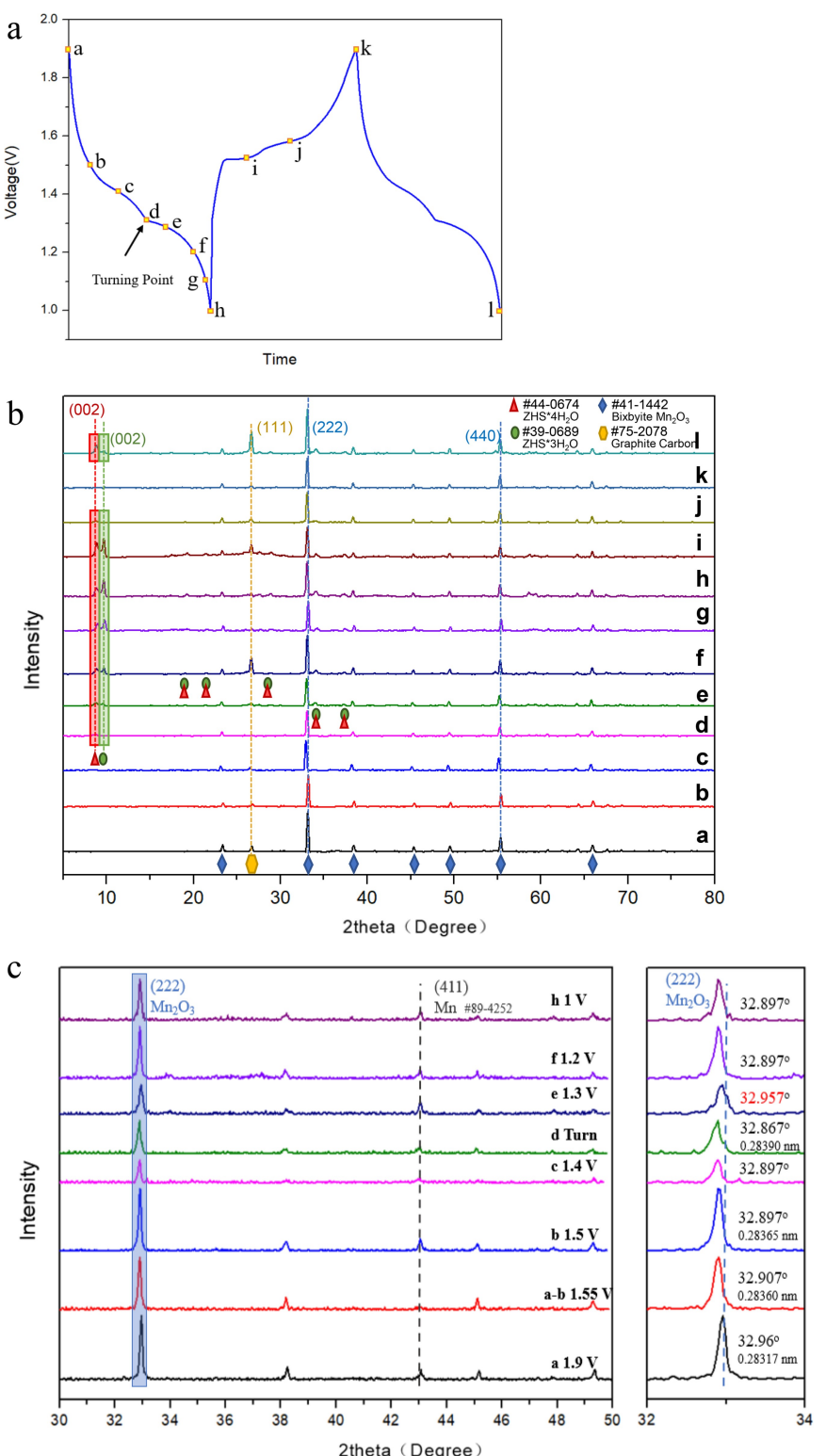


**Figure 3.** a) GCD curve for the 15<sup>th</sup> (discharge only) and 16<sup>th</sup> (charge and discharge) cycles at 200 mA g<sup>-1</sup>. b) XRD patterns of the cathode for the stages indicated in (a). c) XRD patterns of the cathode for the discharge conditions in (b) for the 2-theta range of 30° to 50°; the patterns are further enlarged on the right displaying the 2-theta range of 32° to 34° making the (222) peak from Mn<sub>2</sub>O<sub>3</sub> more visible. Note the (411) peak for Mn, which was used as an internal standard to quantify any Mn<sub>2</sub>O<sub>3</sub> peak shifting.

the (222) peak of Mn<sub>2</sub>O<sub>3</sub> is only 0.00048 nm, which represents ~0.18% change in the d-spacing. Considering that the ionic radii of the H<sup>+</sup> and Zn<sup>2+</sup> ions are 208 pm and 88 pm,

respectively, the amount of intercalation appears to be limited. The primary mechanism responsible for the 1<sup>st</sup> discharge

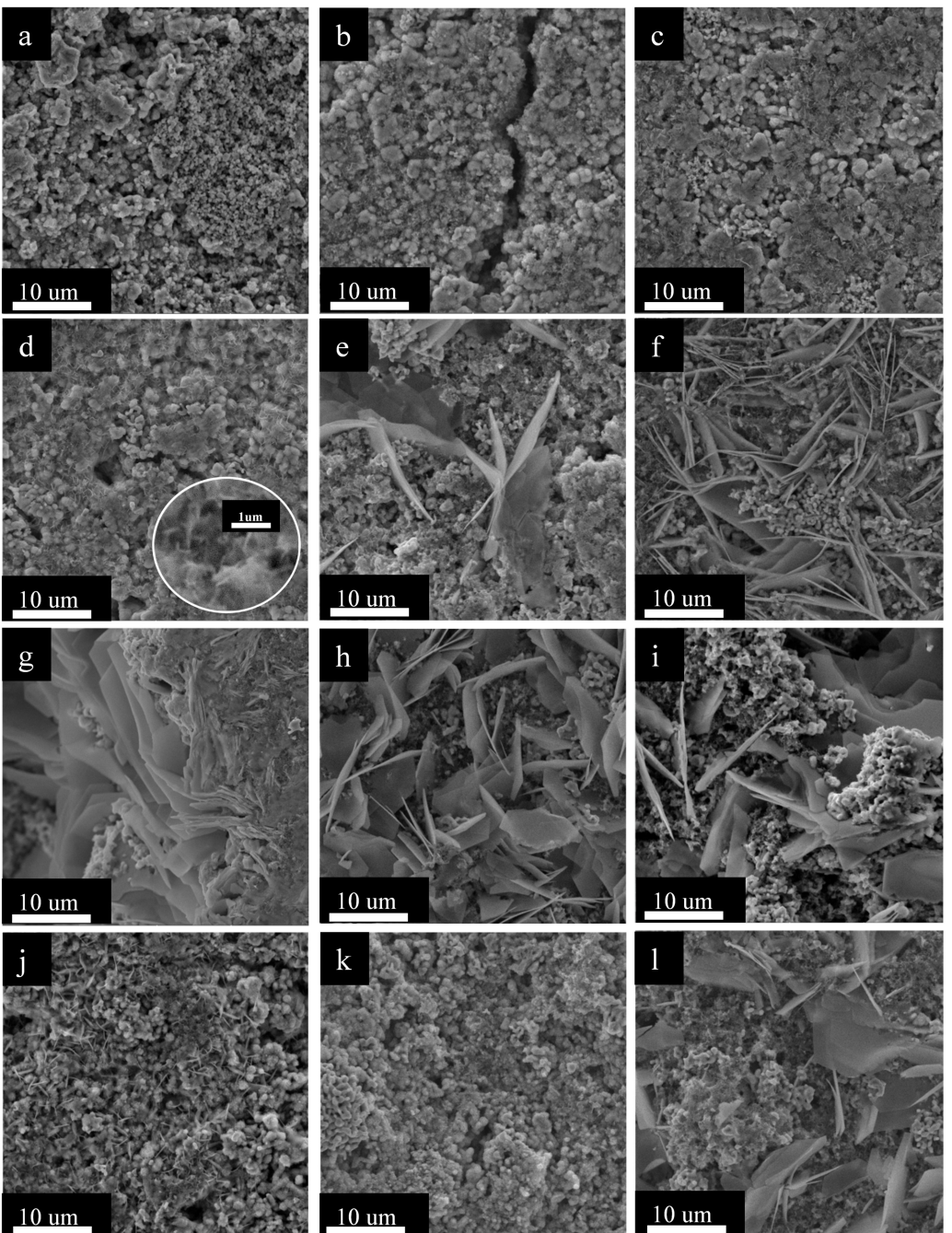


**Figure 4.** Ex-situ SEM images for the various stages shown in Figure 3 during GCD at  $200 \text{ mA g}^{-1}$ . a) Fully charged state of the 15<sup>th</sup> cycle; b) before the first discharge plateau of the 15<sup>th</sup> cycle; c) first discharge plateau of the 15<sup>th</sup> cycle; d) turning point between the two discharge plateaus of the 15<sup>th</sup> cycle; e) second discharge plateau of the 15<sup>th</sup> cycle; f) after the second discharge plateau of the 15<sup>th</sup> cycle; g) close to full discharge of the 15<sup>th</sup> cycle; h) fully discharged state of the 15<sup>th</sup> cycle; i) first charge plateau of the 16<sup>th</sup> cycle; j) second charge plateau of the 16<sup>th</sup> cycle; k) fully charged state of the 16<sup>th</sup> cycle; l) fully discharged stage of the 16<sup>th</sup> cycle.

plateau is likely some other process and will be addressed in subsequent paragraphs.

Further microstructural characterization of select samples was done using TEM/STEM analysis (Figure 5). The samples include the first discharge plateau during the 15th cycle (Figure 5a – position (c) in Figure 3a), the second discharge plateau during the 15th cycle (Figure 5b – position (e) in Figure 3a), the fully discharged state during the 15th cycle

(Figure 5c – position (h) in Figure 3a), the first charge plateau during the 16th cycle (Figure 6a – position (i) in Figure 3a), and the fully charged state during the 16th cycle (Figure 6b – position (k) in Figure 3a). For all samples, STEM bright field (BF) images, STEM annular dark field (ADF) images, EDS maps, and electron diffraction patterns were obtained.

Figure 5a shows a sample from the 1<sup>st</sup> discharge plateau (position (c)).  $\text{Mn}_2\text{O}_3$  particles are surrounded by another phase

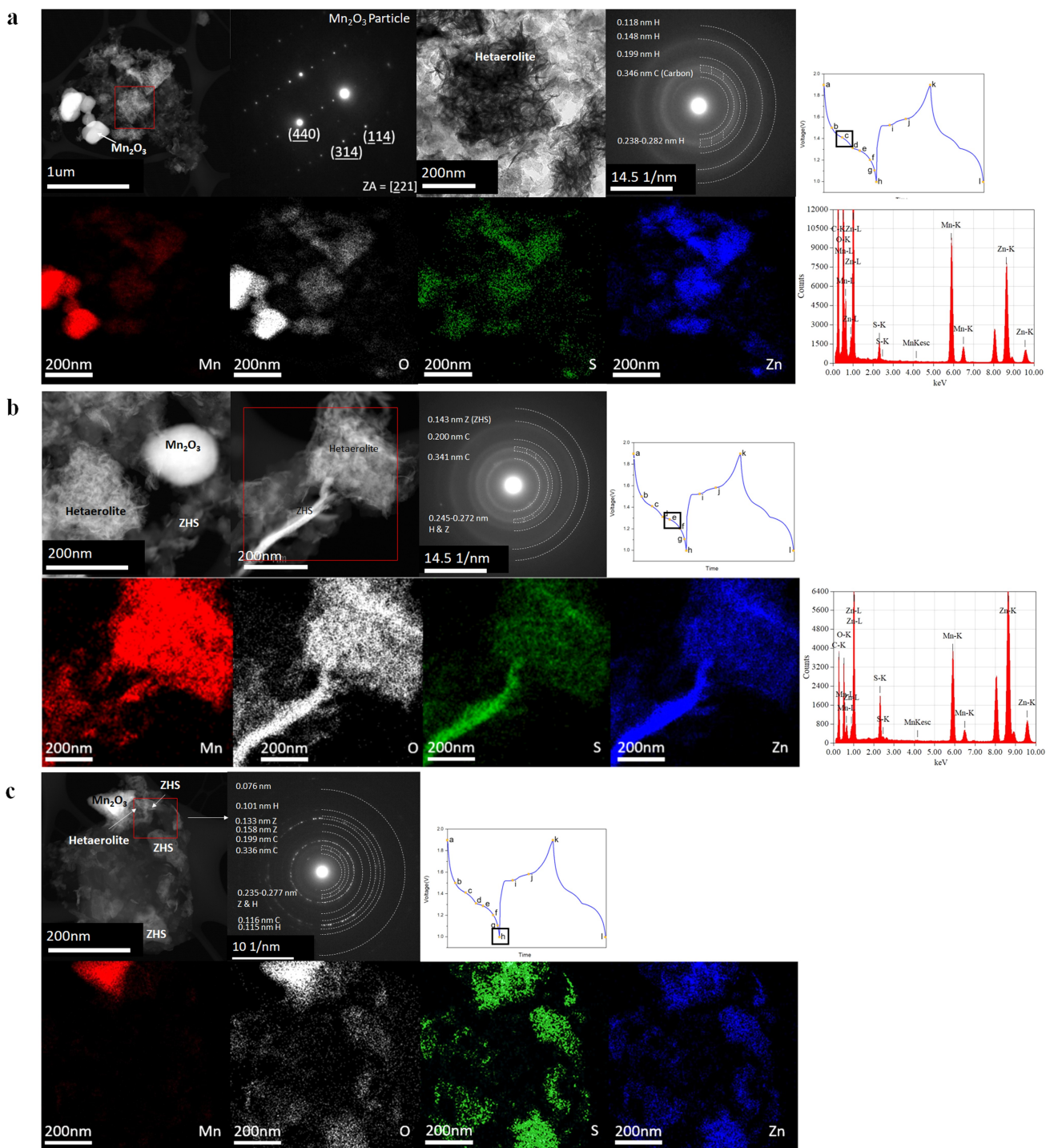


**Figure 5.** Ex-situ STEM ADF images, EDS maps, overall EDS spectra, and SAED patterns of the  $\text{Mn}_2\text{O}_3$  electrode at different stages of discharge: a) First discharge plateau of the 15<sup>th</sup> cycle (position (c)); b) second discharge plateau of the 15<sup>th</sup> cycle (position (e)); c) fully discharged state of the 15<sup>th</sup> cycle (position (h)). Note that the C, H, and Z labels for the diffraction patterns correspond to carbon, hetaerolite, and ZHS, respectively.

which contains Mn, Zn, and O, with smaller amounts of S. An enlarged BF image and an SAED pattern from the red box in the ADF image are also shown. Similar diffraction patterns were obtained from other regions of this sample. Several diffuse rings are present, which indicate that the region is poorly crystalline making indexing difficult. The pattern could not be indexed to any known Zn-S-O or Mn-Zn-S-O phases. The

overall EDS spectrum for the enlarged region shows that the major peaks are Mn, Zn, and O, with a much less intense S peak. Since the S concentration is low, it is likely residual S from the electrolyte, which means that the new phase essentially contains Mn, Zn, and O. Attempts were made to index the SAED to known Mn-Zn-O phases; the best fit was to hetaerolite ( $\text{ZnMn}_2\text{O}_4$ , JCPDS 23-1113 – Figure S7) which is

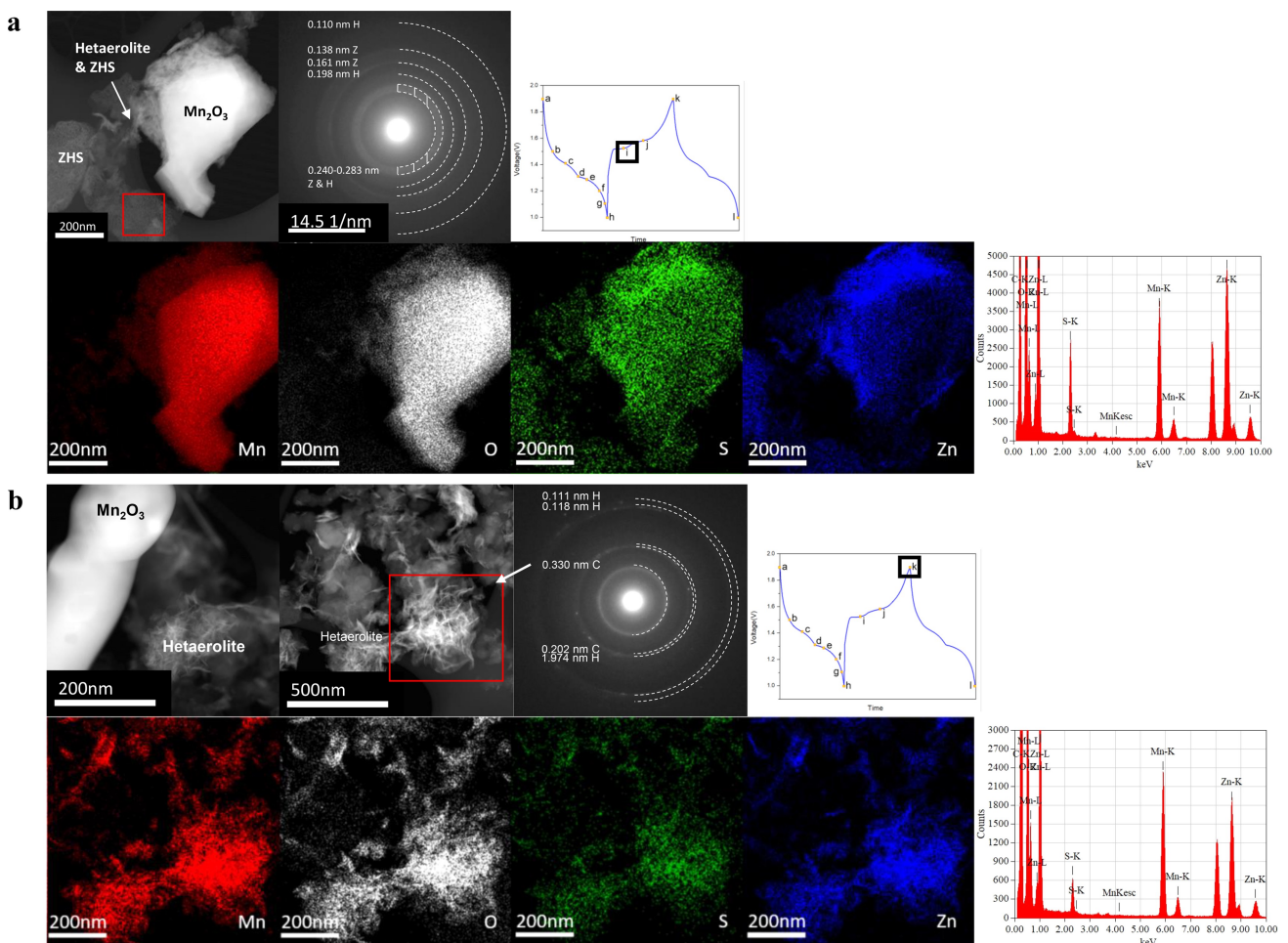


**Figure 6.** Ex-situ STEM ADF images, EDS maps, overall EDS spectra, and SAED patterns of the Mn<sub>2</sub>O<sub>3</sub> electrode at different stages of charge: a) First charge plateau of the 16<sup>th</sup> cycle (position (i)); b) fully charged state of the 16<sup>th</sup> cycle (position (k)). Note that the C, H, and Z labels for the diffraction patterns correspond to carbon, hetaerolite, and ZHS, respectively.

isostructural with hausmannite (Mn<sub>3</sub>O<sub>4</sub>). One of the rings in the SAED pattern (0.346 nm) corresponds to carbon from the electrode. There is a band of rings with a d-spacing range of ~0.238 to 0.282 nm, which corresponds to multiple d-spacings for hetaerolite and are highlighted in the PDF card for hetaerolite shown in Figure S7. More detailed indexing of the electron diffraction pattern is shown in Figure S8. Further discussion of hetaerolite formation will be provided in a later section. Hetaerolite was not identified in the XRD patterns (Figure 3) and this will be addressed a bit later in the paper.

Figure 5b shows two regions of a sample from the 2<sup>nd</sup> discharge plateau (position (e)). For the first STEM ADF image, a Mn<sub>2</sub>O<sub>3</sub> particle, as well as the Mn-Zn-O phase, identified in the previous paragraph as hetaerolite, are present. There is an additional phase, which is likely ZHS that was identified by XRD (Figure 3b) and SEM (large flakes in Figure 4) analysis. The second STEM ADF image in Figure 5b shows hetaerolite as well as one of the ZHS flakes. The EDS maps and overall EDS spectrum, from the second image, show strong Zn, S, and O signals with little or no Mn signal for the flake, which corresponds to ZHS. The SAED pattern from the second image

has diffraction rings that can be indexed to both hetaerolite and ZHS.

The fully discharged state (position (h)) is shown in Figure 5c. EDS maps and an SAED pattern from the enlarged region, indicated by the square, are also shown. This region is mostly ZHS with a Mn<sub>2</sub>O<sub>3</sub> particle (top LHS of the STEM ADF image). There is still hetaerolite distributed between the ZHS regions, which means that hetaerolite does not decompose at lower discharge potentials.

A STEM ADF image of the sample from the 1<sup>st</sup> charge plateau (position (i) – cycle 16) is shown in Figure 6a. Hetaerolite partially surrounds an Mn<sub>2</sub>O<sub>3</sub> particle, with ZHS in the lower left portion of the image (EDS spectra). The SAED pattern has rings that can be indexed to both hetaerolite and ZHS. Note the same band of rings (from ~0.240 to 0.283 nm) which appeared in the other SAED patterns with hetaerolite. The results indicate that hetaerolite is still present and ZHS has not completely decomposed at this point, which is consistent with the XRD and SEM results (Figures 3b and 4i).

A sample corresponding to the fully charge state (position (k)) is shown in Figure 6b. The first image shows Mn<sub>2</sub>O<sub>3</sub> with some hetaerolite adjacent to it, which indicates that hetaerolite

formation is not fully reversible. The second image shows another region of hetaerolite, including an SAED pattern and EDS maps and an overall EDS spectrum. The Mn and Zn signals are strong, while the S signal is weaker and is likely residual S from the electrolyte as mentioned previously.

The TEM/STEM results essentially corroborate the XRD results.  $Mn_2O_3$  particles were observed for all discharge/charge states and were confirmed through EDX mapping and electron diffraction. There was no clear evidence of  $Zn^{2+}/H^+$  intercalation in  $Mn_2O_3$ , although the XRD results showed a slight shift of the  $Mn_2O_3$  peaks to lower angles which could be an indication of limited intercalation – perhaps  $Zn^{2+}$  and/or  $H^+$ . ZHS was detected by both XRD and TEM analysis. A poorly crystalline Mn-Zn-O rich phase (hetaerolite) was identified from the TEM analysis; it first appeared in the first discharge plateau sample, remained throughout discharge, and did not fully decompose on charging.

Hetaerolite was not detected during the XRD analysis, which was due in part to the poor crystallinity of the phase. However, electron diffraction patterns with a band of multiple diffuse rings, corresponding to a range of d-spacings from  $\sim 0.230$  nm to  $\sim 0.280$  nm, were obtained. The band of d-spacings (0.230 nm to 0.280 nm) would correspond to 2-theta values of  $\sim 31.9^\circ$  to  $\sim 39.1^\circ$  in the XRD patterns. Within this angular range, several reflections for  $Mn_2O_3$  and ZHS appear, including two major reflections ((222) and (400)) for bixbyite  $Mn_2O_3$  at  $32.9^\circ$  and  $38.2^\circ$  and several minor reflections for ZHS. These ZHS reflections are indicated by the blue shaded regions in Figures S4 and S5. The hetaerolite electron diffraction patterns also have rings with d-spacings (in decreasing order) of about 0.199–0.204 nm, 0.117 nm, 0.115 nm, 0.111–0.112 nm, and 0.101–0.103 nm. These d-spacings would correspond to 2-theta values for XRD of about  $44.6^\circ$  to  $45.5^\circ$ ,  $82.6^\circ$ ,  $84.1^\circ$  and over  $85^\circ$ . Peaks at  $45.1^\circ$ – $45.3^\circ$  overlap with or are very close to the (332) plane for  $Mn_2O_3$  and the (010) plane for graphitic carbon, leading to interference. In addition, the Mn-Zn-O phase is poorly crystalline so sharp, intense XRD peaks are unlikely. Peaks at 2-theta angles exceeding  $80^\circ$  are out of the 2-theta angular range examined by XRD (Figure 3b). As such, additional X-ray scans were done in the 2-theta angular range of  $80$ – $85^\circ$  for select samples and the patterns are shown in Figure 7. Two weak peaks are visible at  $82.5^\circ$  and  $83.9^\circ$  2-theta, which correlate with the SAED rings with d-spacings of 0.117 nm and 0.115 nm and can be indexed to hetaerolite (316) and (008) crystal planes. The two hetaerolite peaks are also present for the rest of the discharge states and the initial charge states, but are weak for the fully charged state (position (a)).

Further confirmation for the formation of hetaerolite was obtained by preparing an electrode with Ti as the current collector. All previous electrodes used carbon as the current collector, which resulted in carbon being mixed with the electrode material ( $Mn_2O_3$  plus any phases that formed during discharge). Note that TEM samples were prepared by scraping the electrode material from the current collector which invariably led to some carbon being removed as well and carbon rings appearing in SAED patterns. The use of Ti as the

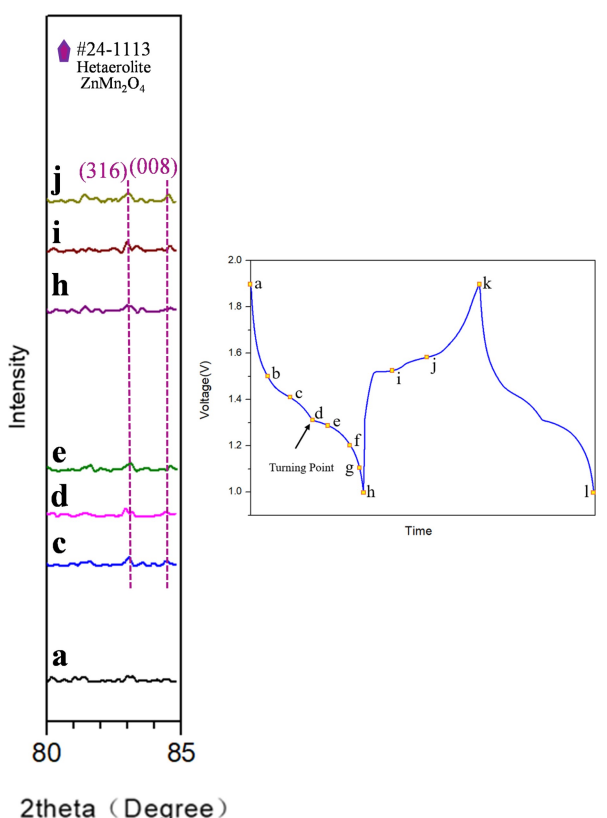
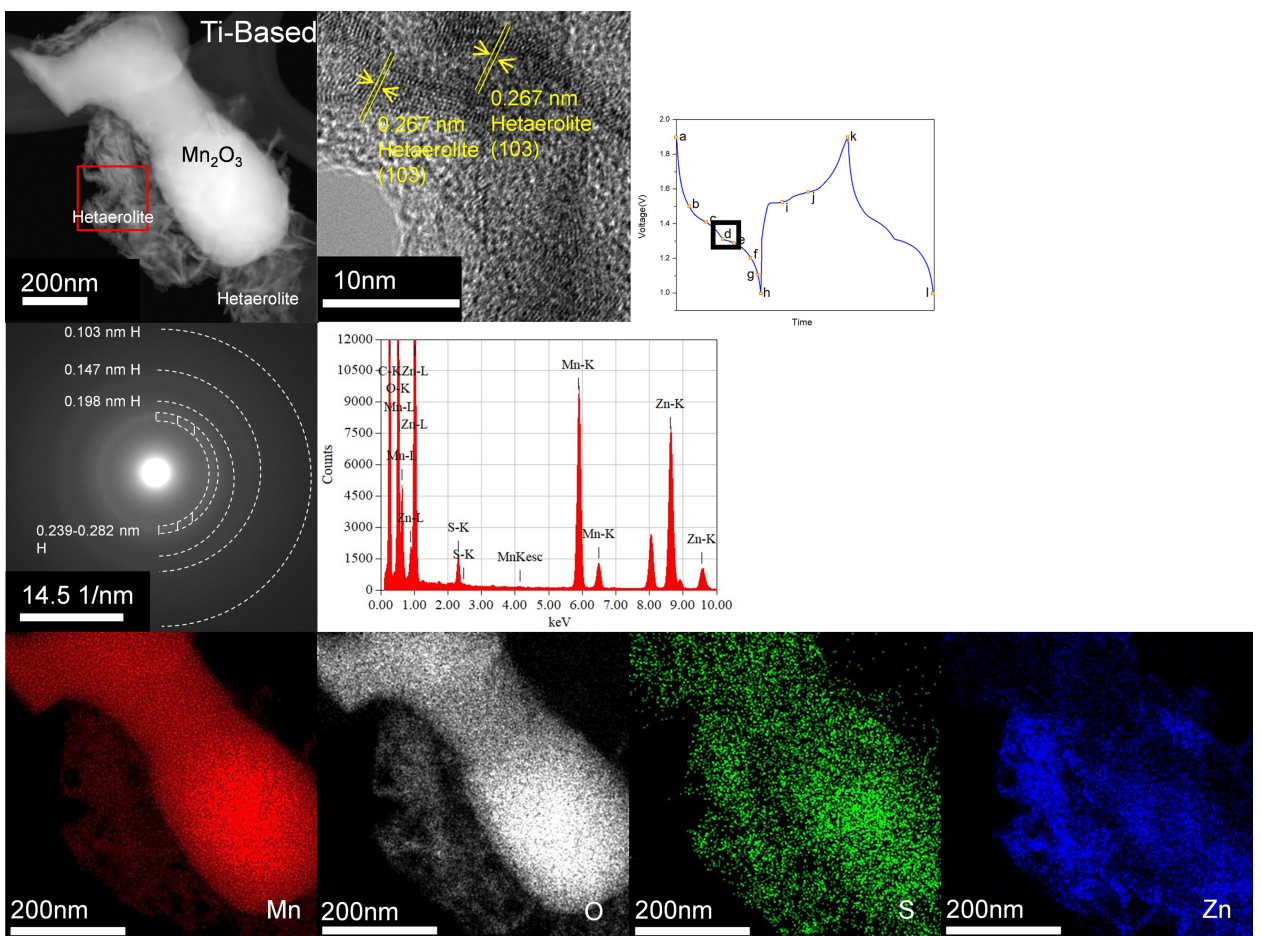


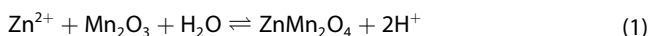
Figure 7. XRD patterns of the cathode for 2-theta in the  $80^\circ$  to  $85^\circ$  range for the stages shown.

current collector eliminated this carbon source. Figure 8 shows a sample from the discharge turning point (position (d) of the 15<sup>th</sup> cycle) of an electrode with a Ti foil current collector. A  $Mn_2O_3$  oxide particle is visible and is surrounded by hetaerolite, which was confirmed by the SAED pattern and EDS analysis. A high resolution (HR) TEM image from part of the hetaerolite is also shown. The poor crystallinity of the hetaerolite phase is evident, although there are localized crystalline regions. The d-spacing of 0.267 nm corresponds to (103) planes for hetaerolite. Figure S9 shows additional TEM analysis for the fully discharged (15<sup>th</sup> cycle) and fully charged states (16<sup>th</sup> cycle) for electrodes with a Ti current collector. Regions with hetaerolite were identified in both cases.

Based on the microstructural analysis and electrochemical results, the following discharge/charge processes are proposed. During initial discharge (from position (a) to position (b) in Figure 3a), there appears to be some intercalation. This could be  $H^+$  and/or  $Zn^{2+}$  ions. The amount of shift is small (the d-spacing increases from 0.28317 nm to 0.28365–0.28390 nm or less than 0.2% change) and remains about the same as discharge proceeds. In any case, the amount of intercalation is minimal. As discharge continues, from position (b) through (c) and (d) (the first plateau in Figure 3a), hetaerolite forms through a chemical conversion reaction with bixbyite ( $Mn_2O_3$ ). There are no electrons involved.



**Figure 8.** Ex-situ STEM ADF image, EDS maps, overall EDS spectrum, SAED pattern, and HRTEM image of the electrode with a Ti current collector at position (d) (turning point) of discharge for the 15<sup>th</sup> cycle.



This reaction has been identified by Rubel et al.<sup>[24]</sup> in their study on the electrochemical stability of ZnMn<sub>2</sub>O<sub>4</sub>. Their

proposed Mn–Zn–H<sub>2</sub>O Pourbaix diagram is redrawn in part in Figure 9 for the pH range of 3 to 8, where line 1 corresponds to Equation (1). Note that potentials utilized during discharge in this work correspond to a range of 1.9 V to 1.0 V vs. Zn/Zn<sup>2+</sup>

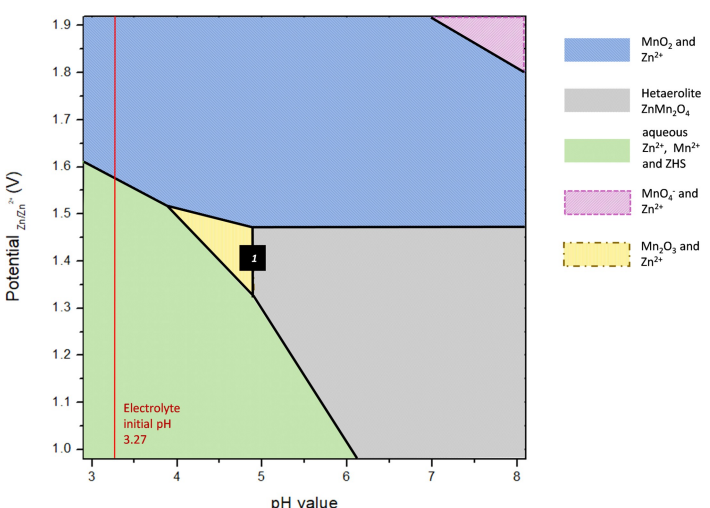
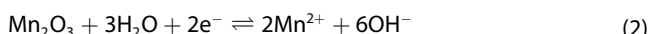
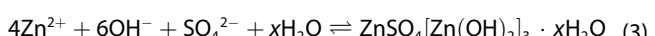


**Figure 9.** Mn–Zn–H<sub>2</sub>O Pourbaix diagram with ZnMn<sub>2</sub>O<sub>4</sub> phase boundaries; redrawn from Ref. [24].

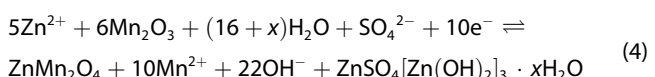
and the initial pH of the electrolyte is 3.27 (labeled as a vertical line in Figure 9). Based on the Pourbaix diagram, decomposition of  $\text{Mn}_2\text{O}_3$  to hetaerolite ( $\text{ZnMn}_2\text{O}_4$ ) occurs at pH values close to 5 and above. The increase in pH needed for the reaction could occur through the partial dissolution of  $\text{Mn}_2\text{O}_3$ , which generates hydroxyl ions.



As discharge continues, from position (d) through the 2<sup>nd</sup> plateau at positions (e) and (f) and finally to position (h) (Figure 3a), ZHS forms according to the following chemical reaction:<sup>[23]</sup>



The overall cathode and anode reactions during discharge can then be written as:



To confirm the hypothesis that the source of hydroxyl ions is manganese oxide dissolution, a rotating ring-disk electrode (RRDE) test was performed. The RRDE test was set up by utilizing the  $\text{Mn}_2\text{O}_3$ -based electrode as the working electrode and monitoring the current from the ring electrode. During linear sweep voltammetry (LSV) of the disk electrode, the reaction products are swept to the outer ring electrode by rotation of the motor. The potentiostat can monitor the current generated by the product at the ring electrode. The LSV curve and corresponding ring electrode current, obtained by scanning from the open circuit potential (OCV) of 1.4 V to 0.9 V, are shown in Figure 10. The Pt ring electrode was maintained at 1.91 V to ensure that any aqueous  $\text{Mn}^{2+}$  ions produced by the

dissolution reaction are oxidized back to  $\text{Mn}^{3+}$ . A significant current is detected on the ring electrode at ~1.36 V, which corresponds to the onset of significant Mn dissolution and the potential of the 1<sup>st</sup> discharge plateau. The current continues to increase during the discharge process which suggests that Mn oxide dissolution occurs throughout the entire discharge process. Manganese oxide dissolution during discharge can locally increase the pH value in the vicinity of the  $\text{Mn}_2\text{O}_3$  electrode. When the pH value reaches a high enough value,  $\text{Mn}_2\text{O}_3$  can transform to hetaerolite.

$\text{Mn}_2\text{O}_3$  dissolution during battery cycling was confirmed through atomic absorption spectroscopy (AAS) measurements (Figure 11). Samples of the electrolyte were analyzed at various fully charged states of cycling, from 0 to 50 cycles where 0 cycles correspond to the pristine electrolyte before testing. Note that the original Mn concentration in the electrolyte, as measured by AAS, is 0.2143 M which is close to the 0.2 M concentration of  $\text{MnSO}_4$  added. With cycling, there is a clear increase in Mn concentration in the electrolyte, which not only indicates that  $\text{Mn}_2\text{O}_3$  dissolution is occurring but that the dissolution reaction (Equation (2)) above is not fully reversible. The accumulation of Mn in the electrolyte during cycling will affect the battery performance and cyclability.

There have been several previous studies that have examined the use of  $\text{Mn}_2\text{O}_3$  as the cathode for ZIBs.<sup>[14–20]</sup> The mechanisms proposed in these studies are summarized in Table 2 and discussed in the following paragraphs in relation to the results from the current study. Note that for all these studies, the CV and GCD curves are similar with two plateaus during both the discharge and charge processes. In addition, the researchers all propose that the discharge process involves some type of intercalation of  $\text{Zn}^{2+}$  and/or  $\text{H}^+$  ions. This is in contrast to our work, where intercalation is not a major contributor to the discharge process. Instead, both plateaus are proposed to be due to chemical processes, involving the formation/decomposition of hetaerolite ( $\text{ZnMn}_2\text{O}_4$ ) and zinc sulphate hydroxide (ZHS).

The initial work done on  $\text{Mn}_2\text{O}_3$  electrodes was by Jiang et al. in 2017.<sup>[14]</sup> They reported the formation during discharge

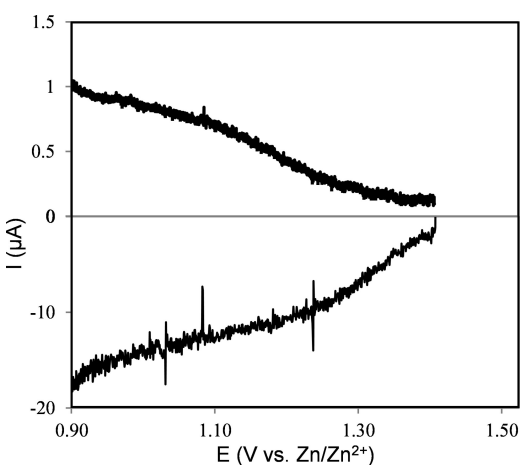


Figure 10. RRDE profile for the  $\text{Mn}_2\text{O}_3$  electrode with a scan rate at 1 mV s<sup>-1</sup> in 2 M  $\text{ZnSO}_4$  + 0.2 M  $\text{MnSO}_4$  solution, stirred at 900 rpm with the Pt ring electrode maintained at 1.91 V vs.  $\text{Zn}/\text{Zn}^{2+}$ .

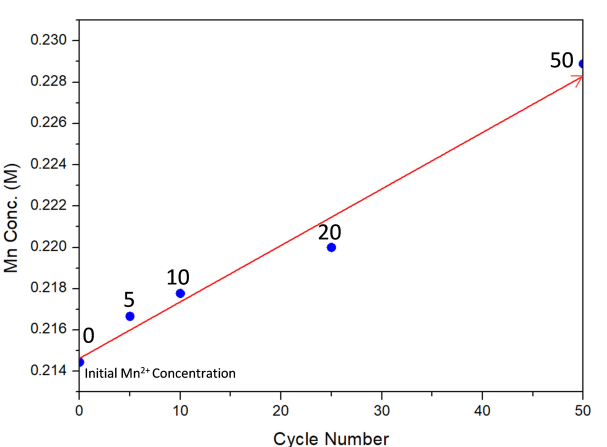


Figure 11. AAS results showing the Mn concentration in the electrolyte after various battery cycles.

**Table 2.** Charge storage mechanism comparison for this work and previous studies of bixbyite Mn<sub>2</sub>O<sub>3</sub> as the cathode for ZIBs.

Author Name	Cathode	Anode	Potential Window	Electrolyte	Charge Storage Mechanisms
Jiang et al. <sup>[14]</sup>	Mn <sub>2</sub> O <sub>3</sub> (cubic)	Zn metal	1–1.9 V	2 M ZnSO <sub>4</sub>	• Mn <sub>2</sub> O <sub>3</sub> transformed to layered-type Zn-birnessite • Zn ion intercalation/extraction
Mao et al. <sup>[15]</sup>	Mn <sub>2</sub> O <sub>3</sub> (cubic)	Zn metal	0.9–1.9 V	2 M ZnSO <sub>4</sub> + 0.2 M MnSO <sub>4</sub>	• Mn <sub>2</sub> O <sub>3</sub> transformed to layered-type Zn-birnessite • Zn <sup>2+</sup> and H <sup>+</sup> intercalation/extraction
Feng et al. <sup>[16]</sup>	Mn <sub>2</sub> O <sub>3</sub> (ortho)	Zn metal	1–1.8 V	2 M ZnSO <sub>4</sub> + 0.2 M MnSO <sub>4</sub>	• MnO formed during H <sup>+</sup> intercalation • ZHS formation • Zn <sup>2+</sup> and H <sup>+</sup> intercalation/extraction
Shen et al. <sup>[17]</sup>	Mn <sub>2</sub> O <sub>3</sub> (cubic)	Zn metal	1–1.9 V	2 M ZnSO <sub>4</sub> + 0.1 M MnSO <sub>4</sub>	• Zn <sup>2+</sup> and H <sup>+</sup> intercalation/extraction
Ma et al. <sup>[18]</sup>	Mn <sub>2</sub> O <sub>3</sub> (cubic)	Zn metal	0.8–1.9 V	3 M ZnSO <sub>4</sub> + 0.2 M MnSO <sub>4</sub>	• Birnessite MnO <sub>2</sub> formed during cycling and acted as a host for Zn <sup>2+</sup> and H <sup>+</sup> intercalation/extraction • ZHS formation
Liu et al. <sup>[19]</sup>	Mn <sub>2</sub> O <sub>3</sub> with oxygen defects (O <sub>Cu</sub> -Mn <sub>2</sub> O <sub>3</sub> ) (cubic)	Zn metal	1–1.8 V	3 M ZnSO <sub>4</sub> + 0.2 M MnSO <sub>4</sub>	• Zn <sup>2+</sup> and H <sup>+</sup> intercalation/extraction with Zn <sub>x</sub> Mn <sub>2</sub> O <sub>3</sub> formation • ZHS formation
Yang et al. <sup>[20]</sup>	Mn <sub>2</sub> O <sub>3</sub> (cubic)/ZnMn <sub>2</sub> O <sub>4</sub> (#23-1113)	Zn Metal	0.8–1.9 V	1 M ZnSO <sub>4</sub>	• Mn <sub>2</sub> O <sub>3</sub> transformed to layered-type Zn-birnessite • ZnMn <sub>2</sub> O <sub>4</sub> listed as energy storage cathode
This work	Mn <sub>2</sub> O <sub>3</sub> (cubic)	Zn Metal	1–1.9 V	2 M ZnSO <sub>4</sub> + 0.2 M MnSO <sub>4</sub>	• Hetearolite formation and ZHS formation (chemical reactions)

of flake-like features on the surface of the Mn<sub>2</sub>O<sub>3</sub> electrode; these are very similar in appearance to the flakes on our electrodes which were identified as ZHS. They attributed the flakes to layered Zn-birnessite, which was proposed to form from the original a-Mn<sub>2</sub>O<sub>3</sub> through intercalation. Their identification was based on XRD analysis of the electrode before and after discharge. After discharge, three additional peaks at 12.2° (0.725 nm), 25.3° (0.352 nm), and 35.0° (0.256 nm) were present relative to the pristine electrode. These peaks were identified as belonging to Zn-birnessite, although the manner in which the pattern was indexed was not shown. The three peaks could be also indexed to ZHS, as was shown in this work. In addition, Jiang et al. only showed EDX analysis from one particle in the TEM with no electron diffraction; EDX analysis in the SEM over a larger region would have been more convincing. Jiang et al also claimed that their electrode was fully reversible, i.e., the Mn<sub>2</sub>O<sub>3</sub> to Zn-birnessite reaction; however, weak peaks at 25.3° and 35.0° remained after full charging. One difference between Jiang et al's work and this work is that their electrolyte did not contain MnSO<sub>4</sub>, which is interesting because the absence of MnSO<sub>4</sub> in the electrolyte would likely enhance Mn dissolution, making ZHS formation more likely.

Feng et al also examined Mn<sub>2</sub>O<sub>3</sub> as the electrode for ZIBs.<sup>[16]</sup> They claimed that their Mn<sub>2</sub>O<sub>3</sub> had an orthorhombic crystal structure; however, their XRD pattern matches well with the cubic form (bixbyite, PDF #41-1442) which is the stable form of Mn<sub>2</sub>O<sub>3</sub>. All other references,<sup>[14–20]</sup> as well as the current work, show that Mn<sub>2</sub>O<sub>3</sub> has the more common cubic structure. Their capacity curves are similar in shape to the ones in this work and those by Jiang et al.<sup>[14]</sup> as well as the other references. Only one SEM image of the electrode was shown along with several TEM images of limited areas. Feng et al. propose that Zn<sup>2+</sup> is

reversibly removed from the electrode, based on XPS and XRD data. The XPS results indicate a Mn<sup>3+</sup>/Mn<sup>2+</sup> ratio of ~2 before discharge. This is puzzling, since the pristine material should have a Mn valence of 3+. For the XRD patterns, Feng et al report that the Mn<sub>2</sub>O<sub>3</sub> peaks shift to lower angles during discharge, which they attribute to lattice expansion due to Zn<sup>2+</sup> intercalation. This may be the case; however, there is no indication that the patterns were calibrated with some type of standard. The XRD patterns in this work were calibrated using Mn powder, specifically the (411) reflection, to ensure that any peak shifts were not due to measurement errors. Feng et al also report that orthorhombic MnO forms during discharge, although the stable form of MnO is cubic (NaCl-type structure). This assertion is based on XRD peaks at 35.2° (0.255 nm), 52.5° (0.174 nm), and 58.0° (0.159 nm). The closest orthorhombic MnO peaks are at 36.4°, 52.6°, and 58.6°, corresponding to (021), (201), and (152) planes, respectively. These peaks could be indexed to ZHS. Feng et al. have indicated that ZHS forms during discharge, but they provided no images to show the morphology. In addition, the lowest 2-theta angle in their XRD patterns is 30°, which is not low enough to show the major ZHS peaks which appear at 2-theta less than 10°. Their TEM images supposedly show MnO, based on lattice measurement spacings, but there are no EDX spectra or electron diffraction patterns for confirmation. In the end, the authors propose that during discharge that there is a combination of Zn<sup>2+</sup> intercalation in Mn<sub>2</sub>O<sub>3</sub>, MnO formation, and ZHS formation with all processes being reversible.

A recent study on Mn<sub>2</sub>O<sub>3</sub> was published by Mao et al.<sup>[15]</sup> They report both H<sup>+</sup> and Zn<sup>2+</sup> ion insertion into Mn<sub>2</sub>O<sub>3</sub> during discharge, with H<sup>+</sup> insertion occurring at higher voltages (1<sup>st</sup> plateau) and Zn<sup>2+</sup> insertion at lower voltages (2<sup>nd</sup> plateau).

Their evidence for  $Zn^{2+}$  intercalation is a “large” shift of the (222) and (400) peaks for  $Mn_2O_3$  to lower angles in the XRD patterns. The shift is only  $\sim 0.6\%$ , which brings into question whether the shift is actually large. In addition, there is no indication that the XRD patterns were calibrated to ensure that shift measurements are indeed real. Their XRD patterns show extra peaks at  $\sim 10^\circ$ ,  $15^\circ$ ,  $20^\circ$ , and  $25^\circ$  2-theta, which they attribute to the intercalated structure, but they did not index those peaks to any particular structure. Their SEM images, after discharge, show numerous surface flakes which are claimed to be the Zn intercalated phase. There is no EDX analysis to support this. The flakes resemble the ZHS flakes seen in our work and the work by Jiang et al.<sup>[14]</sup> They also claim that Zn sulfate forms at lower potentials and current densities.

Ma et al. have investigated the intercalation mechanism in bixbyite ( $\alpha$ - $Mn_2O_3$ ).<sup>[18]</sup> Their electrolyte had a higher  $ZnSO_4$  concentration (3 M) than this work and others and utilized a stainless steel current collector. Their mechanism study focused on the 1<sup>st</sup> discharge/charge and 2<sup>nd</sup> discharge/charge cycles. Their 1<sup>st</sup> discharge cycle had only one plateau, with two plateaus for subsequent cycles. For the 1<sup>st</sup> discharge cycle, they report that  $Mn_2O_3$  undergoes an irreversible transition to L- $Zn_xMnO_2$  (involves partial reduction of Mn from 3+ to 2+) coupled with  $Mn^{2+}$  and  $OH^-$  dissolution leading to ZHS formation. As with other researchers, Ma et al. used XRD to study the discharge/charge processes. During discharge, three new peaks appeared at 2-theta angles of  $12.7^\circ$  (0.697 nm),  $25.4^\circ$  (0.350 nm), and  $37.2^\circ$  (0.242 nm), which were attributed to layered L- $Zn_xMnO_2$ . Three other new peaks also appeared, at  $8.5^\circ$  (1.040 nm),  $33.8^\circ$  (0.265 nm), and  $25.2^\circ$  to  $29.5^\circ$  (0.353 nm to 0.303 nm) and were attributed to ZHS. The capacity for the 2<sup>nd</sup> discharge cycle was slightly higher than that for the 1<sup>st</sup> discharge cycle, which was explained as being due to an amorphous Mn (4+) compound. The layered-type L- $Zn_xMnO_2$  that formed allowed for reversible  $Zn^{2+}$  de-/intercalation during further cycles. This reversible process occurs along with repeated dissolution-deposition of  $Mn^{2+}$  on the cathode surface and  $H^+$  insertion/extraction. A self-regulating process of electrolyte assisted formation/dissolution of flake-like ZHS occurs as well. Ma et al also report that  $MnO_2$ , derived from L- $Zn_xMnO_2$  and  $Mn^{2+}$  dissolved in the electrolyte, is the actual host for the intercalation of  $H^+$ , rather than  $\alpha$ - $Mn_2O_3$  itself.

Liu et al developed  $Mn_2O_3$  with oxygen defects by introducing Cu ions.<sup>[19]</sup> Their material was synthesized hydrothermally and utilized 3 M  $ZnSO_4$  as the electrolyte in the battery. They proposed a  $H^+/Zn^{2+}$  ion insertion charge storage mechanism based mostly on XRD data. Based on their GCD discharge curve and XRD patterns, ZHS formation started at 1.6 V during discharge, which means the ZHS formation reaction started as soon as the battery was discharged and occurred continuously to the fully discharged state (1 V). Their cell cycling potential window was 1–1.8 V. They proposed that ZHS formation is due to leftover  $OH^-$  in the electrolyte after  $H^+$  intercalation in  $Mn_2O_3$ . However, they provide no other supporting evidence for  $H^+$  intercalation. Three peaks, at  $\sim 28^\circ$  (0.320 nm),  $\sim 34^\circ$  (0.264 nm), and  $\sim 37^\circ$  (0.244 nm) 2-theta, from their XRD pattern of the fully discharged state (1 V) were

attributed to  $Zn_xMn_2O_3$  which is proposed to form by  $Zn^{2+}$  ion insertion. However, no PDF card was provided to support the indexing of the peaks. The XRD patterns also had two intense peaks below  $10^\circ$  2-theta, indicating that at least two types of ZHS formed, but the authors only specified one type (ZHS·5H<sub>2</sub>O). The peaks that the authors indexed to  $Zn_xMn_2O_3$  could also be indexed to ZHS·4H<sub>2</sub>O ((106), (312) and (134) – PDF #44-0673) or ZHS·3H<sub>2</sub>O ((114), (312) and (314) – PDF #39-0689).

There are two other papers that have examined  $Mn_2O_3$  electrodes. In both cases, there was no detailed microstructural analysis; the authors referenced the work by Jiang et al when proposing mechanisms. In the work by Shen et al.,<sup>[17]</sup>  $MnO_2$  was compared with  $Mn_2O_3$  and the two potential plateaus during discharge of  $Mn_2O_3$  are claimed to be due to  $H^+$  and  $Zn^{2+}$  ion insertion, respectively.<sup>[17]</sup> Yang et al.<sup>[20]</sup> synthesized a composite material of  $ZnMn_2O_4/Mn_2O_3$  and claim that  $Mn_2O_3$  undergoes a phase transformation to Zn birnessite ( $ZnMn_2O_3$ ), with  $Zn^{2+}$  intercalation to Zn birnessite being responsible for the charge storage mechanism.

## Conclusions

In this work, highly crystalline  $Mn_2O_3$  (bixbyite) was synthesized via precipitation and calcination and was utilized as the cathode for an aqueous zinc-ion battery (aZIB). Multiple characterization methods were used to determine the morphology and structure of the cathode, before and after cycling. The cells delivered good electrochemical performance, cyclability, and stability. Discharge capacities of tested cells reached as high as  $375\text{ mAh g}^{-1}$  at  $50\text{ mA g}^{-1}$  and  $65\text{ mAh g}^{-1}$  at  $2000\text{ mA g}^{-1}$ . A specific capacity of  $211\text{ mAh g}^{-1}$  was achieved after 200 cycles at a current density of  $500\text{ mA g}^{-1}$ , corresponding to 93% capacity retention. In addition, 73% capacity retention was realized after 1100 cycles at a current density of  $2000\text{ mA g}^{-1}$ . A new energy storage mechanism for bixbyite  $Mn_2O_3$  was proposed. Microstructural analysis, using X-ray diffraction (XRD) and electron microscopy, showed that intercalation of either  $Zn^{2+}$  or  $H^+$  in  $Mn_2O_3$  may occur to some extent but is not the principal mechanism during discharge. Instead, the mechanism proposed here involves two chemical conversion reactions resulting in the formation of hetaerolite ( $ZnMn_2O_4$ ) during the 1<sup>st</sup> discharge plateau followed by zinc hydrate sulfate (ZHS) formation during the 2<sup>nd</sup> discharge plateau. Capacity fading during cycling of the  $Mn_2O_3$  electrode is linked to  $Mn_2O_3$  dissolution and incomplete reversibility of the hetaerolite reaction.

## Experimental Section

### Material synthesis

An acidic metal sulfate solution was prepared, consisting of 0.1 M manganese sulfate monohydrate ( $MnSO_4 \cdot H_2O$ ,  $\geq 99\%$ ) dissolved in water (100 mL). The base, aqueous solution consisted of 100 mL sodium hydroxide (NaOH,  $\geq 99\%$ ) and ammonia ( $NH_3 \cdot H_2O$ , 28–

30%) with a molar ratio of NaOH:NH<sub>3</sub>·H<sub>2</sub>O = 2.4 (0.2 M NaOH). The starting solution was obtained by dissolving NaOH and NH<sub>3</sub>·H<sub>2</sub>O (NaOH:NH<sub>3</sub>·H<sub>2</sub>O = 2.4, 1 M NaOH) in water (40 mL) with the pH carefully adjusted to 10.5 using sulfuric acid (H<sub>2</sub>SO<sub>4</sub>, 2 M). The acidic MnSO<sub>4</sub> solution and the base solution were slowly added to the starting solution at a rate of  $\approx$  2 mL min<sup>-1</sup>. The pH (10.5  $\pm$  0.3) was maintained until the reaction was complete. The brown precipitates were then collected by filtration and dried overnight in a vacuum oven at 70 °C. The resulting precursor powder was transferred to a box furnace and calcined in air at 800 °C for 10 h.

### Electrochemical measurements

Electrodes were prepared by uniformly spreading a slurry (N-methyl-2-pyrrolidone as the solvent) containing the active material (70 wt%), acetylene carbon (20 wt%), and polyvinylidene fluoride (pVdF, 10 wt%) as the binder and then casting on carbon paper (graphite carbon current collector) or a Ti film with a thickness of 80  $\mu$ m. The electrodes were then dried overnight at 120 °C in a vacuum oven. The final electrodes were sectioned into circular pieces with a mass loading of  $\sim$  2 mg cm<sup>-2</sup>. CR2032 coin cells were assembled in air using the Mn<sub>2</sub>O<sub>3</sub> composite cathode, zinc foil as the anode, Whatman glass fiber paper (GF/D) as the separator, and 2 M ZnSO<sub>4</sub> with 0.2 M MnSO<sub>4</sub> aqueous solution as the electrolyte. The coin cells were electrochemically tested using BioLogic SP-300 and VSP-300 potentiostats. Cyclic voltammetry (CV) and galvanostatic discharge-charge (GCD) profiles were obtained from 1 V to 1.9 V vs. Zn/Zn<sup>2+</sup> at multiple scan rates and current densities. A rotating ring-disk electrode (RRDE) was used to investigate the reaction mechanisms during charge and discharge. A Pine Research rotator (AFMSRCE), a rotating electrode controller, and a fixed disk RRDE tip were utilized.

### Materials characterization

X-ray diffraction (XRD – Rigaku Ultima IV), with a Cu K $\alpha$  ( $\lambda$  = 1.54056 Å) X-ray source, was utilized to examine the crystal structure of the samples. Oxidation states of the elements in the material were determined using X-ray photoelectron spectroscopy (XPS), via an Al-K $\alpha$  X-ray source with a pass energy of 20 eV (Kratos AXIS Supra XPS Instrument). The spectra were calibrated using the carbon peak at 284.8 eV. Scanning electron microscopy (Tescan Vega3 SEM, operated at 20 kV) and energy dispersive X-ray spectroscopy (EDS) were used to characterize the microstructure and composition of the fabricated samples. Transmission/scanning transmission electron microscopy (JEOL JEM-ARM 200CF TEM/STEM, operated at 200 kV) and EDS mapping were also employed to examine the microstructure and composition of samples at higher magnifications, as well as to generate additional crystal structure information. Atomic absorption spectroscopy (AAS – ThermoFisher iCE 3500) was used to determine the Mn ion concentration within the electrolyte.

### Acknowledgements

The authors are grateful to the Natural Sciences and Engineering Research Council (NSERC RGPIN-2018-04488) of Canada for research funding. The authors would also like to acknowledge the contributions and support from Dr. Wendy Tran (RRDE, XPS), Dr. Shiraz Merali (AAS), Dr. Anqiang He (XRD), Ms. Zahra Abedi (XRD), and Mr. Matthew Labbe (battery testing).

### Conflict of Interest

The authors declare no conflict of interest.

### Data Availability Statement

The data that support the findings of this study are available from the corresponding author upon reasonable request.

**Keywords:** aqueous electrolyte • bixbyite Mn<sub>2</sub>O<sub>3</sub> • cathode material • energy storage mechanism • zinc-ion batteries

- [1] E. E. McDuffie, R. V. Martin, J. V. Spadaro, R. Burnett, S. J. Smith, P. O'Rourke, M. S. Hammer, A. van Donkelaar, L. Bindle, V. Shah, L. Jaeglé, G. Luo, F. Yu, J. A. Adeniran, J. Lin, M. Brauer, *Nat. Commun.* **2021**, *12*, 1.
- [2] A. Z. AL Shaqsi, K. Sopian, A. Al-Hinai, *Energy Rep.* **2020**, *6*, 288.
- [3] N. Alias, A. A. Mohamad, *J. Power Sources* **2015**, *274*, 237.
- [4] T. Kim, W. Song, D.-Y. Son, L. K. Ono, Y. Qi, *J. Mater. Chem. A* **2019**, *7*, 2942.
- [5] G. J. May, A. Davidson, B. Monahov, *J. Energy Storage* **2018**, *15*, 145.
- [6] C. Jeyaseelan, A. Jain, P. Khurana, D. Kumar, S. Thatai, in *Rechargeable Batteries: History, Progress, and Applications*, R. Boddula, I. Inamuddin, R. Pothu, and A. M. Asiri, eds. John Wiley and Sons (Hoboken, NJ, USA) and Scrivener Publishing (Beverly, MA, USA), **2020**, 177–194.
- [7] H. Kim, J. Hong, K.-Y. Park, H. Kim, S.-W. Kim, K. Kang, *Chem. Rev.* **2014**, *114*, 11788.
- [8] G. J. May, A. Davidson, B. Monahov, *J. Energy Storage* **2018**, *15*, 145.
- [9] M. Mahmud, N. Huda, S. Farjana, C. Lang, *Batteries* **2019**, *5*, 22.
- [10] Y. Zhang, Y. Liu, H.-Y. Ye, D.-W. Fu, W. Gao, H. Ma, Z. Liu, Y. Liu, W. Zhang, J. Li, G.-L. Yuan, R.-G. Xiong, *Angew. Chem.* **2014**, *126*, 5164.
- [11] C. Yang, X. Ji, X. Fan, T. Gao, L. Suo, F. Wang, W. Sun, J. Chen, L. Chen, F. Han, L. Miao, K. Xu, K. Gerasopoulos, C. Wang, *Adv. Mater.* **2017**, *29*, 1701972.
- [12] N. D. Ingale, J. W. Gallaway, M. Nyce, A. Couzis, S. Banerjee, *J. Power Sources* **2015**, *276*, 7.
- [13] M. Song, H. Tan, D. Chao, H. J. Fan, *Adv. Funct. Mater.* **2018**, *28*, 1802564.
- [14] B. Jiang, C. Xu, C. Wu, L. Dong, J. Li, F. Kang, *Electrochim. Acta* **2017**, *229*, 422.
- [15] M. Mao, X. Wu, Y. Hu, Q. Yuan, Y.-B. He, F. Kang, *J. Energy Chem.* **2021**, *52*, 277.
- [16] D. Feng, T.-N. Gao, L. Zhang, B. Guo, S. Song, Z.-A. Qiao, S. Dai, *Nano-Micro Lett.* **2019**, *12*.
- [17] H. Shen, B. Liu, Z. Nie, Z. Li, S. Jin, Y. Huang, H. Zhou, *RSC Adv.* **2021**, *11*, 14408.
- [18] Y. Ma, Y. Ma, T. Dimant, K. Cao, X. Liu, U. Kaiser, R. J. Behm, A. Varzi, S. Passerini, *Adv. Energy Mater.* **2021**, *11*, 2100962.
- [19] N. Liu, X. Wu, Y. Yin, A. Chen, C. Zhao, Z. Guo, L. Fan, N. Zhang, *ACS Appl. Mater. Interfaces* **2020**, *12*, 28199.
- [20] S. Yang, M. Zhang, X. Wu, X. Wu, F. Zeng, Y. Li, S. Duan, D. Fan, Y. Yang, X. Wu, *J. Electroanal. Chem.* **2019**, *832*, 69.
- [21] M. C. Biesinger, B. P. Payne, A. P. Grosvenor, L. W. M. Lau, A. R. Gerson, R. S. C. Smart, *Appl. Surf. Sci.* **2011**, *257*, 2717.
- [22] E. S. Ilton, J. E. Post, P. J. Heaney, F. T. Ling, S. N. Kerisit, *Appl. Surf. Sci.* **2016**, *366*, 475.
- [23] B. Lee, H. R. Seo, H. R. Lee, C. S. Yoon, J. H. Kim, K. Y. Chung, B. W. Cho, S. H. Oh, *ChemSusChem* **2016**, *9*, 2948.
- [24] O. Rubel, T. N. T. Tran, S. Gourley, S. Anand, A. V. Bommel, B. D. Adams, D. G. Ivey, D. Higgins, *arXiv preprint arXiv:2203.10175* **2022**, <https://doi.org/10.48550/arXiv.2203.10175>.

Manuscript received: April 22, 2022

Revised manuscript received: June 17, 2022

Accepted manuscript online: June 19, 2022

Version of record online: July 14, 2022